The sodium tungsten bronzes as plasmonic materials: fabrication, calculation and characterization

Levi Tegg[1], Dylan Cuskelly[2] and Vicki J Keast[1]

[1] School of Mathematical and Physical Sciences, University of Newcastle, Callaghan, NSW 2308, Australia.

[2] School of Engineering, University of Newcastle, Callaghan, NSW 2308, Australia

Email: levi.tegg@uon.edu.au

Abstract

The tungsten bronzes are non-stoichiometric transition metal oxides of the form M_xWO_3, where $0 \leq x \leq 1$, and M is a dopant ion, most commonly an alkali metal. In this work, the sodium tungsten bronzes (Na_xWO_3) are investigated as materials for plasmonic applications. The bronzes were fabricated with a solid state reaction, the dielectric function calculated using density functional theory (DFT) and the nanoparticle responses calculated with the boundary element method (BEM). The results were compared to Au and Ag, the materials most widely used in plasmonic applications. It was shown that for $x > 0.5$, the solid state fabrication method produces cube-shaped particles of diameter ≥ 1 μm, whose bulk optical properties are well described by a free-electron model and a rigid band structure. The addition of Na into the lattice increases the free electron density, increasing the bulk plasma frequency. Nanoparticle plasmon resonances are found to be highly tunable, and generally at a lower frequency than Au or Ag, and so sodium tungsten bronzes are predicted to be well suited to biomedical or chemical sensing applications.

Keywords: tungsten bronzes, plasmonic materials, plasmonic sensors, nanocubes

1. Introduction

The field of plasmonics has presented solutions to problems in a variety of disciplines, including photovoltaics [1], oncology [2], chemical sensing [3,4], and photocatalysis [5]. Localized surface plasmon resonances (LSPRs) occur when light incident on a metal nanoparticle couples into the resonant modes of the particle, which are defined by the particle geometry and the optical properties of the material(s) from which the particle is constructed. For a given geometry, the materials dielectric function, $\varepsilon(\omega) = \varepsilon_1(\omega) + i\varepsilon_2(\omega)$, will determine the allowed LSPRs. In brief, the real part ε_1 will set the frequencies at which plasmons can occur, and the imaginary part ε_2 determines damping [6]. For applications involving the use of nanostructures or nanoparticles, an ideal plasmonic material should have optical properties such that $\varepsilon_2 \approx 0$ in the frequency range where $\varepsilon_1 \leq -2$, depending on the geometry of the particle.

Au and Ag are the current materials of choice for plasmonic applications. However, broad interband transitions limit the use of Au above $\omega \approx 2$ eV, whereas significant chemical reactivity limits the applications of Ag [7,8]. There is a need for plasmonic materials which exhibit both high chemical stability and desirable optical properties, preferably over a broad frequency range. Several review articles [7–10] have assessed the potential of alternative materials to advance the field of plasmonic applications. Some recent materials of interest include Au alloys and intermetallics [11–13], transition metal nitrides such as TiN and ZiN [14,15], graphene [16], and heavily doped semiconductors such as ITO, AZO [17,18] or n-type doped Ge thin films [19].

The tungsten bronzes are non-stoichiometric tungsten oxides of the form M_xWO_3, where $0 \leq x \leq 1$ and M is a dopant ion, usually an alkali metal [20–22] and most commonly Na [23–27]. By varying Na content in Na_xWO_3, substantial changes in electrical and optical properties of the material are observed. At low x, the sodium tungsten bronzes behave like semiconductors, and increasing x increases electrical conductivity [25]. The change in conductivity is associated with a dramatic change in colour: at $x = 0$ the material is lime green (arising from interband absorption in WO_3), but sweeps through dark blue, violet, pink, orange and yellow as x is increased to $x = 1$ [26]. This colour change arises from an increase in the bulk plasma frequency (ω_p), where the Na 3s electrons are donated to the W 5d conduction band as x is increased [27]. In contrast to most other metals, the ω_p of the sodium tungsten bronzes falls in the visible frequency range, and is tunable by varying the Na concentration.

The crystal structures for the cubic phases of Na_xWO_3 are shown in figure 1. For $x \approx 0.0$ (a), corner-sharing WO_6 octahedra sit buckled, with each layer of octahedra tilted in alternating directions. As Na is added to the lattice, the octahedra gradually rotate such that the O atoms move towards their ideal cubic perovskite positions [28,29]. At higher Na concentrations, the structural distortions are so slight that the supercell reflections can be difficult to observe in X-ray diffraction (XRD) patterns, and so a unit cell $1/8^{th}$ the volume of that shown in (b) is often reported in the literature [29]. These octahedral rotations and distortions lead to changes in the crystal system symmetry [30], whereby increasing x can change the crystal system from monoclinic (prefixed with m-) at $x \approx 0.0$, to orthorhombic (o-) at $x \approx 0.04$, through two tetragonal phases (a perovskite-like TI- [31] from $0.1 \leq x \leq 0.3$ and a pentagonal tunnel TII- [32] from $0.1 \leq x \leq 0.5$), until the cubic (c-) phase shown in figure 1 for $x > 0.5$. Bronzes fabricated via solid state reaction are generally observed to be mixed phase below $x < 0.5$ [30]. A hexagonal (h-) phase can also be formed via hydrothermal synthesis, where Na ions occupy hexagonal tunnels formed by the WO_3 octahedra [33,34].

In this work, the sodium tungsten bronzes have been investigated for their potential as plasmonic materials. The bronzes have been fabricated by a solid state technique, and characterized in terms of their crystal structure by XRD, their morphology by scanning electron microscopy (SEM) and visible light microscopy (VLM), and their optical properties by spectrophotometry. These results are supported by density functional theory (DFT) calculations of the optical properties, and nanoparticle simulations performed using a boundary element method (BEM). Lastly, the bronzes are compared to Au and Ag, for their suitability for plasmonic applications.

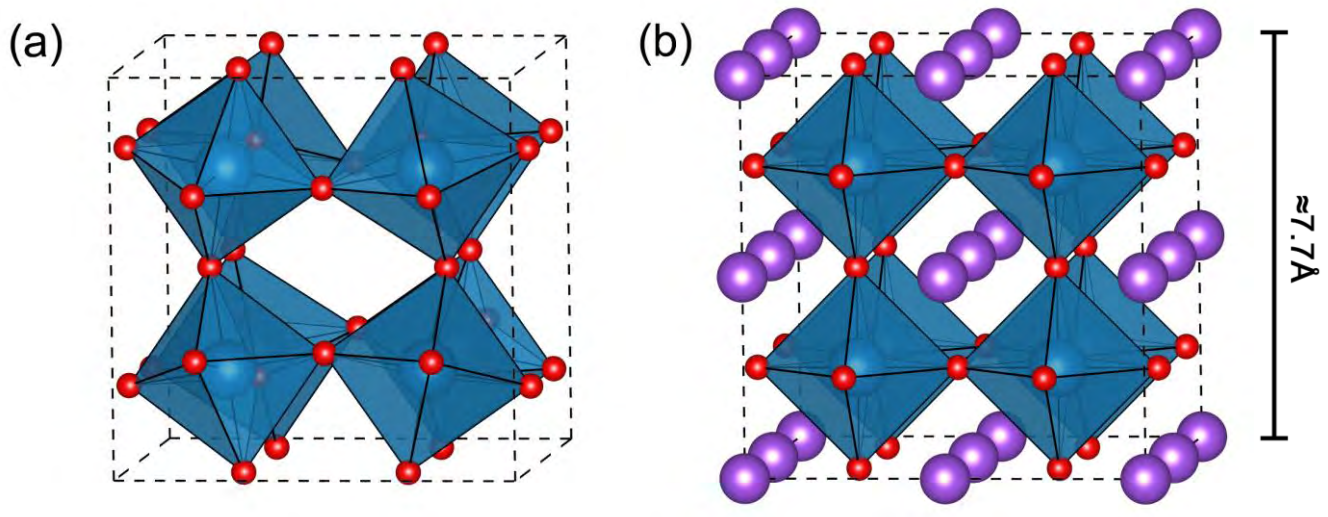

Figure 1. Crystal structures of Na_xWO_3. W atoms and polyhedra are blue, O atoms are red, Na atoms are purple. (a) The WO_6 octahedra in WO_3 ($x \approx 0.0$) are buckled and rotated. (b) Intercalating a dopant ion straightens the octahedra, as in $NaWO_3$. Scale bar shows approximate lattice parameter.

2. Methods

2.1. Fabrication

Samples of sodium tungsten bronze were fabricated using the solid state technique first described by Straumanis [23]. Powders of sodium tungstate dihydrate (Sigma-Aldrich, >99%), tungsten (IV) oxide (Sigma-Aldrich, 99.9%) and tungsten (Sigma-Aldrich, 99.9%) were mixed proportionally for a given x according to the following reaction:

$$\frac{x}{2}(Na_2WO_4 \cdot 2H_2O) + \frac{3-2x}{3}WO_3 + \frac{x}{6}W \rightarrow Na_xWO_3 + xH_2O$$

The starting powders were manually shaken then pressed under 200 MPa into pellets of diameter 15 mm and height ≈ 3 mm. The pellets were loaded into alumina or graphite crucibles, and fired in an alumina tube furnace at 850 °C for 10 hours with a 5 °C.min^{-1} initial ramp, under continuous Ar flow at a rate of approximately 1 cm^3.s^{-1}. Prior to characterization, the samples were crushed by mortar and pestle.

2.2. Characterization

XRD was performed using a Phillips X'Pert MPD XRD with a Cu Kα (λ = 1.541 Å) anode, at 40 kV voltage with 40 mA of current. All samples were analysed for ≈ 30 minutes over $5° \leq 2\theta \leq 90°$ with a 0.013° step size. Phase identification was performed using PANalytical Highscore, drawing from the ICSD [35] and ICDD [36] crystal structure databases. No unidentified peaks were observed in the diffraction patterns. Rietveld refinement was performed using Rietica version 4.2 [37], a frontend to the FORTRAN 77/90 code LHPM [38]. In the refinement, lattice parameters, scale factors, site-occupancy factors, background parameters and peak shapes were refined. A Pseudo-Voight (FCJ asymmetric) peak shape was used, with the U and γ_0 parameters allowed to refine. Quantitative phase analysis (QPA) was performed on the refined phases, using the method of Hill and Howard [38].

Prior to further analysis, all of the samples were washed to dissolve any unreacted Na_2WO_4. Samples were suspended in distilled water and passed through standard qualitative filter paper. The filtrate was discarded, and the

solid powder remaining was then dried before further characterization. VLM was performed on the powdered samples using a Leica DM750P microscope with an attached digital camera. Samples were imaged in bright-field reflection mode, illuminated by white LEDs via the objective lens. SEM was performed using a Zeiss Sigma VP FESEM. Powders of the samples were dispersed onto adhesive carbon tape, and coated in ≈ 40 nm of carbon for imaging. All samples were imaged under a 10 kV beam, using a secondary electron (SE) detector.

To measure optical extinction spectra, suspensions of Na_xWO_3 were produced by re-crushing the fired powders under mortar and pestle to reduce particle sizes further, and then dispersing in distilled water. After the larger particles had settled, the upper levels of the blue-tinted solution were extracted for spectrophotometry. A Cary 6000 UV-Vis Spectrophotometer with an integrating sphere was used to measure the extinction spectra. A wavelength range of 200-1200 nm was scanned in 1 nm steps, with a deuterium plasma lamp for the 200 – 350 nm range, and a tungsten halogen lamp used for the 350 – 1200 nm range.

2.3. Calculation

In this work, c-Na_xWO_3 was modelled with a cubic unit cell across all of $0 \leq x \leq 1$. The 2×2×2 supercell arrangement from figure 1(b) was used, where up to 8 Na atoms could be intercalated into the WO_6 framework to obtain bronzes across $0 \leq x \leq 1$ in $\Delta x = 0.125$ steps. The lattice parameter, space group, and inequivalent atoms used for each calculation are shown in Table 1. The Na atom positions within the unit cell were chosen to maximize symmetry, as ordered arrangements lead to minimal anisotropies in the calculated optical properties. The lattice parameter was set using the linear relation from Brown and Banks, a (Å) = $0.0819x + 3.7846$ [24]. This lattice parameter was then doubled for the supercell arrangement. DFT calculations were performed using the linearized augmented plane-wave plus local orbitals method (LAPW+lo), as implemented in the WIEN2k software package [39]. For the $x = 0.000$ and $x = 1.000$ unit cells, WIEN2k recognized the high crystal symmetry, and reduced the unit cell back to a 1×1×1 arrangement before beginning the calculation, thus halving the lattice parameters. Core states were considered those to be -6.0 Ryd (≈ -81 eV) below the Fermi level (E_F). The maximum angular momentum for the radial wavefunctions was set to $l_{max} = 10.0$, and size of the basis set via $R_{MT}K_{max} = 7.0$. Unoccupied states were calculated up to 7.0 Ryd (≈ 95 eV) above E_F, so as to include a sufficiently large range of interband transitions in the calculation of optical properties. The generalized gradient approximation of Perdew, Burke and Ernzerhof (PBE-GGA) [40] was used as the exchange correlation potential in these calculations. For $0.125 \leq x \leq 0.875$, an 18×18×18 k-point mesh (≈ 6000 k-points in the full Brillouin zone) was used, whereas for $x = 0.000$ and $x = 1.000$, a 36×36×36 mesh (≈ 48000 k-points) was used to compensate for the reduction in the size of the unit cell. Increasing $R_{MT}K_{max}$ and the k-mesh density was tested, and no significant change was observed in the calculated optical properties.

To calculate the optical properties, the random-phase approximation (RPA) was used to calculate the interband contributions to ε_2, from which ε_1 was calculated using Kramers-Kronig integration [41]. In calculating the optical matrix elements, the upper energy range was increased from the default value up to 5.0 Ryd (≈ 68 eV) above E_F to include more of the unoccupied states. Interband transitions were broadened by $\gamma_{IB} = 0.05$ eV. A Drude term was added to ε_2 to account for the metal-like character of the materials, using ω_p calculated by WIEN2k and the scattering parameter $\gamma_{drude} = 0.15$ eV determined from ellipsometry data from the literature [42,43]. The reflectivity

$R(\lambda)$ was calculated from $\varepsilon(\omega)$, and convolved with standard colour matching functions [44] to find an approximate apparent colour for the material in sRGB colour space.

Table 1. Crystal structures used to model c-Na_xWO_3 in this work. For the x = 0.000 and x = 1.000 structures, WIEN2k was used to find the increased symmetry, and reduce the size of the unit cell accordingly.

x	a (Å)	Space Group (IUC Number)	Inequivalent Atom Positions (x/a, y/a, z/a (R_{MT}))		
			W	O	Na
0.000	3.7846	P m -3 m (221)	0.00, 0.00, 0.00 (1.91)	0.50, 0.00, 0.00 (1.64)	-
0.125	7.5897	P m -3 m (221)	0.25, 0.25 ,0.25 (1.92)	0.00, 0.25, 0.25 (1.65) 0.50, 0.25, 0.25 (1.65)	0.00, 0.00, 0.00 (2.50)
0.250	7.6102	I m -3 m (229)	0.75, 0.25, 0.25 (1.92)	0.50, 0.25, 0.25 (1.65)	0.00, 0.00, 0.00 (2.50)
0.375	7.6306	P m -3 m (221)	0.25, 0.25, 0.25 (1.93)	0.00, 0.25, 0.25 (1.66) 0.50, 0.25, 0.25 (1.66)	0.50, 0.00, 0.00 (2.50)
0.500	7.6511	F m -3 m (225)	0.25, 0.25, 0.25 (1.93)	0.00, 0.25, 0.25 (1.66)	0.00, 0.00, 0.00 (2.50)
0.625	7.6716	P m -3 m (221)	0.25, 0.25, 0.25, (1.94)	0.00, 0.25, 0.25 (1.67) 0.50, 0.25, 0.25 (1.67)	0.50, 0.50, 0.50 (2.50) 0.00, 0.00, 0.00 (2.50) 0.50, 0.00, 0.00 (2.50)
0.750	7.6921	I m -3 m (229)	0.75, 0.25, 0.25 (1.94)	0.50, 0.25, 0.25 (1.67)	0.50, 0.00, 0.00 (2.50)
0.875	7.7125	P m -3 m (221)	0.25, 0.25, 0.25 (1.95)	0.00, 0.25, 0.25 (1.68) 0.50, 0.25, 0.25 (1.68)	0.00, 0.00, 0.00 (2.50) 0.50, 0.00, 0.00 (2.50) 0.00, 0.50, 0.50 (2.50)
1.000	3.8665	P m -3 m (221)	0.00, 0.00, 0.00 (1.95)	0.50, 0.00, 0.00 (1.68)	0.50, 0.50, 0.50 (2.50)

Nanoparticle extinction spectra (σ_{ext}) were calculated using the MNPBEM toolbox [45,46], a MATLAB implementation of the boundary-element method (BEM) [47]. In this toolbox, particles are defined by abrupt boundaries, where different materials are defined by isotropic, frequency-varying, dielectric functions $\varepsilon(\omega)$. Discretization occurs only on the surface of the boundary, and not within the nanoparticle or external media volumes. The planewave illumination of nanospheres, nanocubes and nanorods was modelled, with particle diameters ranging from 20 nm to 500 nm, in external media with frequency-invariant and lossless $\varepsilon_{medium} = n_{medium}^2$. In all simulations, the retarded electric field case, invoking the full set of Maxwell equations, was used. Discretization parameters were found by convergence testing. The dielectric functions for Au and Ag were those of Johnson and Christy (JC) [48].

3. Results and discussion

3.1. Crystal Structure and Morphology

Figure 2 shows XRD patterns collected from four of the fabricated Na_xWO_3 samples, with identified phases, the refinement, and the residuals overlaid. Most of the samples comprised of multiple phases: high Na content bronzes ($x \geq 0.7$) were mostly c-Na_xWO_3 with small amounts of Na_2WO_4 (see Table 2 for QPA). In the middle content bronzes ($\approx 0.4 < x < 0.7$), disodium ditungstate ($Na_2W_2O_7$) [49] was observed alongside c-Na_xWO_3 and TII-

Na_xWO_3 [32]. The lower content bronzes ($x \leq 0.4$) were found to be highly mixed-phase, though the TII-Na_xWO_3 phase became dominant, with c-Na_xWO_3 appearing in decreasing amounts. In this work we have focused mainly on the cubic bronze phases, and so will not thoroughly discuss bronzes with $x < 0.3$.

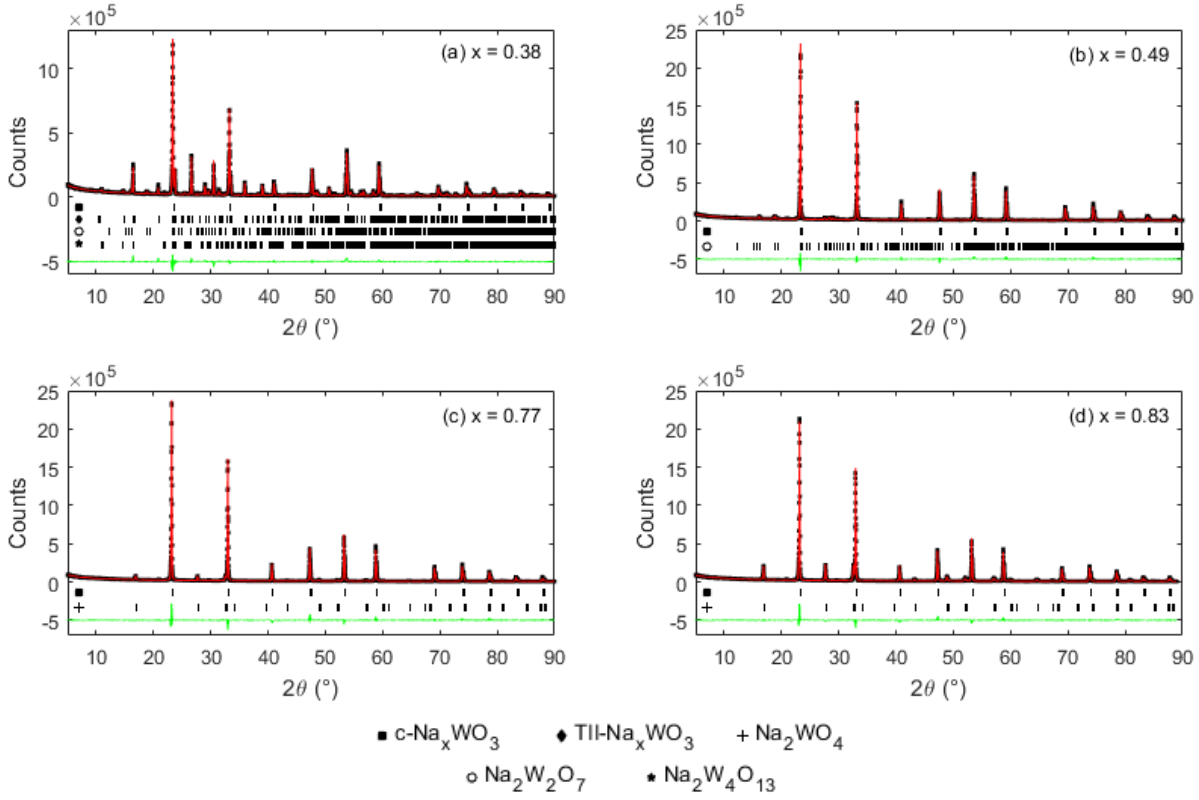

Figure 2: X-ray diffraction patterns and Rietveld refinements for fabricated Na_xWO_3 with (a) $x = 0.38$, (b) $x = 0.49$, (c) $x = 0.77$ and (d) $x = 0.83$. Black dots indicate measured intensities, red line represents the refined pattern, green line represents the residual, and the vertical black lines indicate identified peaks in the refined model for each phase. Peak lists are identified by shapes, where the square represents c-Na_xWO_3, the diamond TII-Na_xWO_3 [32], the plus Na_2WO_4 [50], the circle $Na_2W_2O_7$ [49], and the star $Na_2W_4O_{13}$ [51].

Table 2. Summary of refined parameters and QPA for some of the fabricated samples.

Nominal *x*	**c-Na_xWO_3 *a* (Å)**	**Refined *x***	**Weight Percentage (%W_p) of Phases**					**R_p**	**R_{wp}**	**χ^2**
			c-Na_xWO_3	**TII-Na_xWO_3**	**Na_2WO_4**	**$Na_2W_2O_7$**	**$Na_2W_4O_{13}$**			
0.4	3.8155(3)	0.38	47.9 ± 0.2	44.6 ± 0.2	-	3.8 ± 0.1	3.7 ± 0.1	5.47	7.25	156.4
0.5	3.8248(2)	0.49	93.2 ± 0.2	-	-	6.8 ± 0.1	-	4.90	6.79	143.8
0.6	3.8256(3)	0.50	75.6 ± 0.2	-	-	24.4 ± 0.2	-	5.63	7.88	181.7
0.7	3.8394(2)	0.67	89.7 ± 0.2	-	4.8 ± 0.1	5.6 ± 0.1	-	5.64	7.83	179.2
0.8	3.8475(2)	0.77	94.9 ± 0.2	-	5.1 ± 0.1	-	-	5.64	7.82	191.1
0.9	3.8483(2)	0.78	91.1 ± 0.2	-	8.9 ± 0.1	-	-	5.28	7.15	153.5
1.0	3.8527(2)	0.83	81.9 ± 0.2	-	18.1 ± 0.1	-	-	5.63	7.35	186.5

A summary of the refined parameters is shown in Table 2. The 'nominal *x*' column represents the intended Na content (as per the chemical equation in section 2.1.) before the sample was fired. The 'Refined *x*' column represents the Na content of the c-Na_xWO_3 phase, as calculated from the lattice parameter and the relation from Brown and Banks [24]. The results of the QPA, expressed as weight percentages (%W_p), are also shown. The uncertainties represent the standard deviations calculated by Rietica for each parameter, though the residuals in figure 2 suggest that the true uncertainties are likely higher, particularly for the lower *x* samples where peaks from

multiple phases overlap. The last three columns present the profile (R_p), weighted profile (R_{wp}) and goodness-of-fit (χ^2) parameters for each refinement. The relative proportions of the phases qualitatively match those reported in the literature [24,30], except for the observation of $Na_2W_2O_7$ phase around $x \approx 0.5$ and the $Na_2W_4O_{13}$ phase around $x \approx 0.4$, neither of which have been previously reported as products of these fabrication methods.

In the ≈ 12 months subsequent to fabrication, the samples did not undergo any visible corrosion or degradation. XRD performed after 12 months found no new phases and no significant changes to the patterns presented in this work, which were acquired immediately after fabrication. In addition, the samples have been briefly washed in water and/or ethanol, and no change in appearance or in material properties has been observed, except for the re-crystallization of unreacted and water soluble Na_2WO_4. This suggests that the sodium tungsten bronzes are chemically stable in these environments, which matches reports of high chemical stability in the literature [26,52]. Systematic studies of chemical reactivity and atmospheric degradation are ongoing.

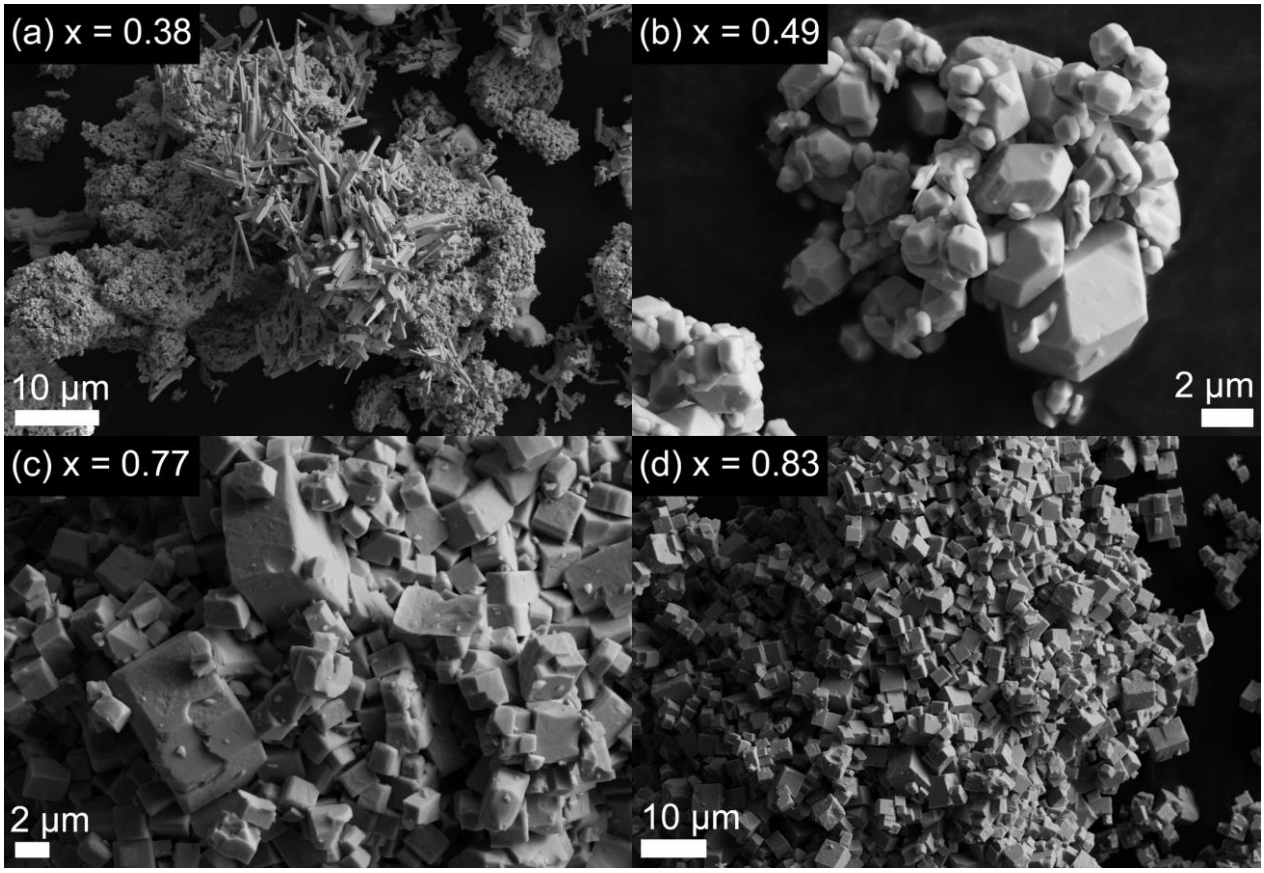

Figure 3. SEM images of four Na_xWO_3 powders, with stoichiometries (a) $x = 0.38$, (b) $x = 0.49$, (c) $x = 0.77$ and (d) $x = 0.83$ for their cubic phases.

Figure 3 shows SEM images of the fabricated bronzes where the c-Na_xWO_3 sodium content is (a) $x = 0.37$, (b) $x = 0.49$ and (c) $x = 0.77$ and (d) $x = 0.83$. The microstructures commonly observed in $x \approx 0.4$ samples (Fig. 3 (a)), are high aspect ratio (≈ 1 µm diameter, >10 µm long) needles interspersed with truncated cubes and tetrahedrons. Around $x \approx 0.5$ (b), the needles no longer appear, and rounded cubes and tetrahedrons of varying diameters become dominant. For $x > 0.7$ (c,d), almost all of the particles observed were sharp cubes of diameter >1 µm. The morphology of the particles is indicative of the phases present in the sample: for $x < 0.4$, Na_xWO_3 forms a number of low-symmetry phases, and is largely mixed phase below $x < 0.3$ [30]. It is believed that the needle structures are

the TII-Na_xWO_3 phase, given the $\%W_p$ of the TII phase in the $x = 0.38$ sample (see Table 2). From $x > 0.4$, cubic crystal systems, appearing either as tetrahedra or cubes, begin to dominate, until around $x > 0.7$, where the cubic perovskite structure shown in figure 1(b) is formed, which leads to sharp cube-shaped particles.

The bronzes in this work were fabricated via a simple furnace-assisted solid-state fabrication technique, first described over 60 years ago [23]. Recent work in the literature on the tungsten bronzes has mainly focused on alternative fabrication techniques, such as fused salt electrolysis [53,54], hydrothermal preparations [33,55–57], microwave-assisted synthesis [34,58], or the use of soda-lime glass as a substrate [59]. Whilst these techniques have proven successful at producing phase-pure tungsten bronze nanoparticles, they are arguably more complex. The technique in this work requires a single qualitative mixing step and a single firing step, producing well-shaped particles down to $d \approx 1$ μm. Work is underway to optimize the machining and firing parameters to reduce this particle size further. The simplicity and effectiveness of this fabrication technique lends to the idea that the process is industrially scalable, which could allow for the production of large volumes of tungsten bronze nanoparticles quickly. Such large scale production processes would facilitate the use of the tungsten bronzes in solar control window coatings, as discussed in section 3.3., and has been suggested recently in the literature [20,60].

Whilst these fabrication methods did not produce completely phase pure Na_xWO_3, the two dominant impurities Na_2WO_4 and $Na_2W_2O_7$ are transparent in the visible-frequency region with band gaps $E_g > 4.0$ eV [61,62], a result our group was able to verify with DFT calculations. Na_2WO_4 is water soluble, and so samples with $x > 0.7$ can be washed to produce phase-pure c-Na_xWO_3. In addition, Ribnick et al [30] showed that the as-fired products could be washed with ammonia, hydrochloric and hydrofluoric acid, which dissolved other impurity phases except for the sodium tungsten bronzes. Regardless, further investigations are underway to fabricate phase pure samples and to determine methods and processes to control stoichiometry.

3.2. Electronic Structure and Optical Properties

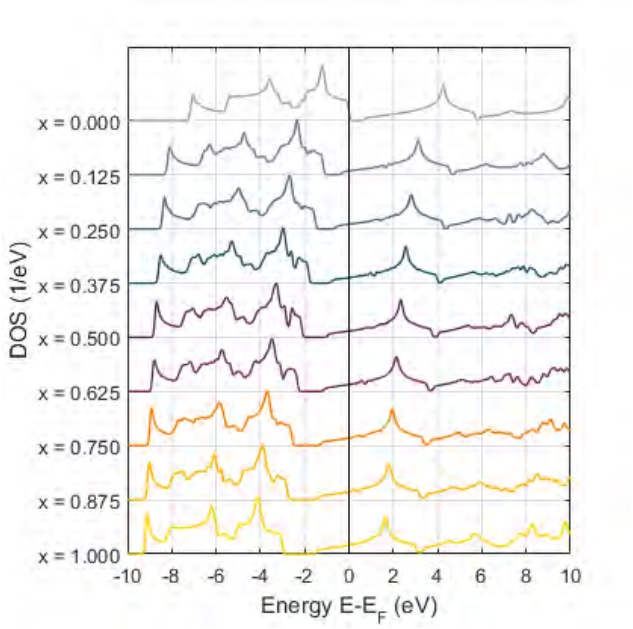

Figure 4. DFT calculated density of states (DOS) for c-Na_xWO_3 for $0.0 \leq x \leq 1.0$ between $-10 \leq E_F \leq +10$ eV. Each DOS is plotted with respect to its own E_F.

The calculated density of states (DOS) between $-10 \leq E_F \leq +10$ eV for Na_xWO_3 for $0 \leq x \leq 1$ is presented in figure 4. For $x \geq 0.125$, the DOS is typical of metals, while for $x = 0.000$, the structure is more typical of a semiconductor. Qualitatively, the overall structure of the DOS around E_F is similar for each stoichiometry, with the biggest change being the value of E_F, which rises further into the conduction band with increasing Na concentration. The valence band is structurally similar for all compositions, though some minor peaks appear around -8 eV, as well as a dip around -2.5 eV. Above +4 eV, the conduction band is quite different between compositions, and whilst the sharp peak just above E_F is always present, the structures $\geq +8$ eV change considerably with increasing Na content. These results suggest that the valence and low-energy conduction bands are well modelled by a rigid band model, with a rising E_F with increasing x. Some of the fine-scale structures in figure 4 can be attributed to the supercell: the low energy edge of the conduction band is smooth for the $x = 0.000$ and 1.000 calculations, but has fine structure around E_F for the others. This is a result of the reduced symmetry of the unit cells, leading to reduced degeneracy. The structure of the DOS presented here for $x = 0.000$ and $x = 1.000$ closely matches that reported in earlier density functional investigations [63,64]. DOS for the other compositions has not previously been reported in the literature.

Figure 5 presents the calculated real (a) and imaginary (b) parts of $\varepsilon(\omega)$ up to $\omega = 10$ eV for c-Na_xWO_3, over $0 \leq x \leq 1$. The Drude-metal behaviour at low energies is evident for $x \geq 0.125$, with ε_1 rising steeply and ε_2 falling quickly with increasing ω. The bulk plasmon frequency (where $\varepsilon_1(\omega_p) = 0$) increases with increasing Na content, from $\omega_p = 1.10$ eV for $x = 0.125$, up to $\omega_p = 2.49$ eV for $x = 1.000$. This can be interpreted in terms of the Drude model, where the addition of Na into the lattice increases the free electron density, which in turn increases the plasma frequency ω_p. A minimum in ε_2 is observed in the visible frequency range, and the centre and width of this minimum increase with increasing Na content. A broad interband peak in the ultraviolet is seen to increase in energy and decrease in width as Na is added to the lattice. It is immediately evident from figure 5 that $\varepsilon_1 \approx -2$ in the frequency range where $\varepsilon_2 \approx 0$, and thus bulk, surface, and localized surface plasmons are expected to occur with high efficiency.

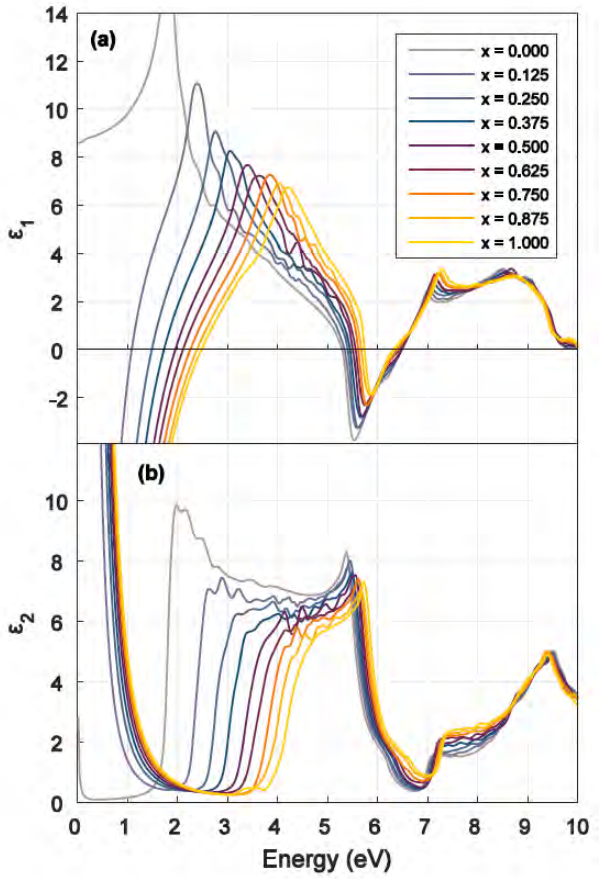

Figure 5. DFT calculated real (a) and imaginary (b) parts of $\varepsilon(\omega)$ up to ω = 10 eV for c-Na_xWO_3 for $0 \leq x \leq 1.0$.

Figure 6 compares the ε(ω) calculated in this work for (a) x = 0.625 and (b) x = 0.875 against dielectric function data from the literature obtained via ellipsometry of single crystals of (a) x = 0.628 and (b) x = 0.860 [42]. There is good agreement with experiment, particularly in the visible frequency range, which is of interest for this work. The energy of the interband transitions at ~ 4 eV is underestimated, as would be expected from our use of the GGA exchange correlation functional [65]. A scissors operator could be used to adjust the energy of these transitions, but the associated change in ε_1 leads to inaccuracies in bulk and nanoparticle plasmon resonance frequencies. These dielectric functions are quantitatively similar to those obtained by other authors, from both electron energy-loss spectroscopy [66] and from optical ellipsometry [43].

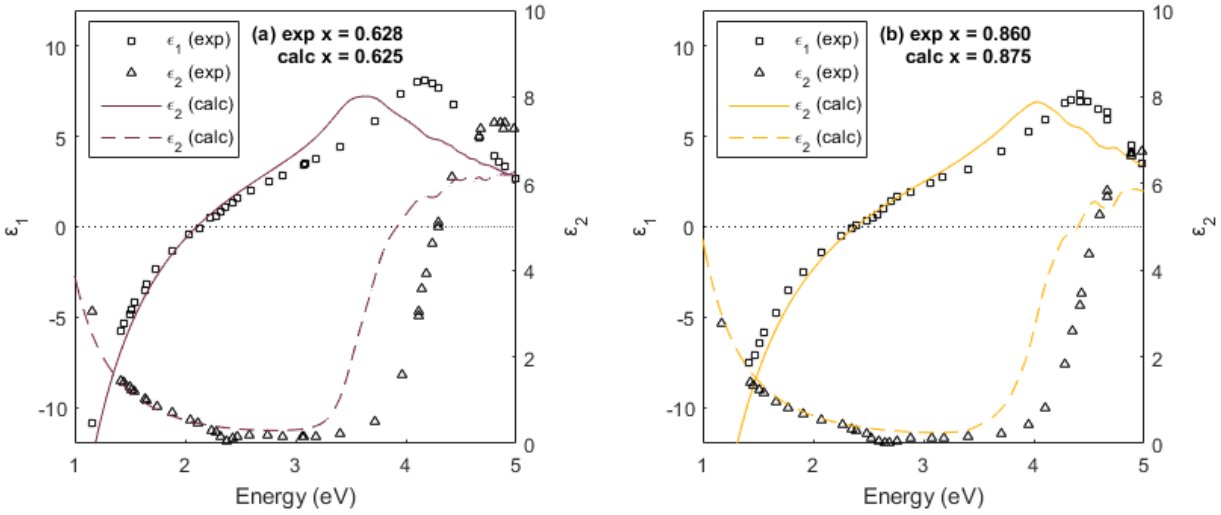

Figure 6. Comparison between experimental and calculated dielectric functions. (a) Experimental results for x = 0.628 are compared to calculated results for x = 0.625. (b) Experimental results for x = 0.860 are compared to calculated results for x = 0.875. Experimental dielectric function from [42]. Solid line and squares represent ε_1, dashed line and triangles represent ε_2. Horizontal dotted line represents $\varepsilon_1 = 0$.

It has been shown that the WO_6 octahedral buckling influences the calculated optical properties in WO_3, with the buckled lattice having a far larger band gap than the ideal perovskite structure [21,67]. To explore this effect in Na_xWO_3, $\varepsilon(\omega)$ for the ideal perovskite structure for x = 0.75 is compared with the experimental buckled structure for x = 0.73 as determined by Wiseman and Dickens [28] in figure 7. It can be seen that differences are subtle, particularly in the 1-3 eV range. These results validate the ideal perovskite approximation made in this work for the high-sodium content bronzes.

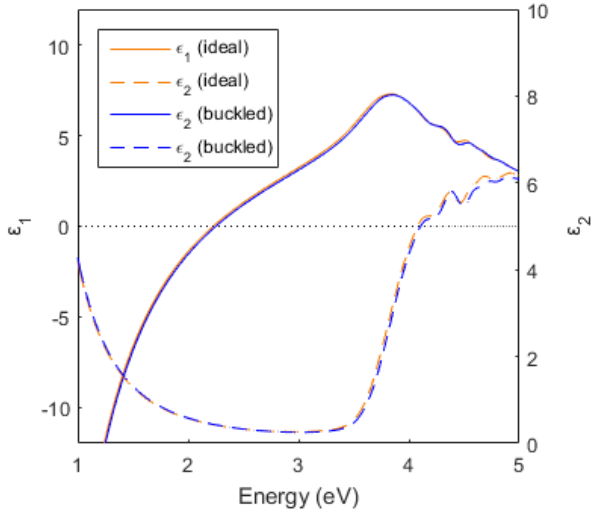

Figure 7. Dielectric function for $Na_{0.75}WO_3$ with an idealised perovskite structure (orange), compared with that of the buckled structure of $Na_{0.73}WO_3$ (blue) [28]. Solid lines represent ε_1, dashed lines represent ε_2. Horizontal dotted line represents $\varepsilon_1 = 0$.

From $\varepsilon(\omega)$, the flat-plane normal-incidence reflectivity for each Na_xWO_3 was calculated, and are shown in figure 8. The reflectance profiles shown for $x \geq 0.125$ are, again, typical of free-electron metals, exhibiting high reflectivity at long wavelengths, a reflectance minimum around the bulk plasma frequency, and increasing reflectivity with shorter wavelengths. It can be seen that the reflectance minimum blue-shifts with increasing Na content as expected from the increasing the bulk plasma frequency ω_p. It is the free-electron character of the bronzes which leads to the broad spectrum of colours observed in the sodium tungsten bronze series [68].

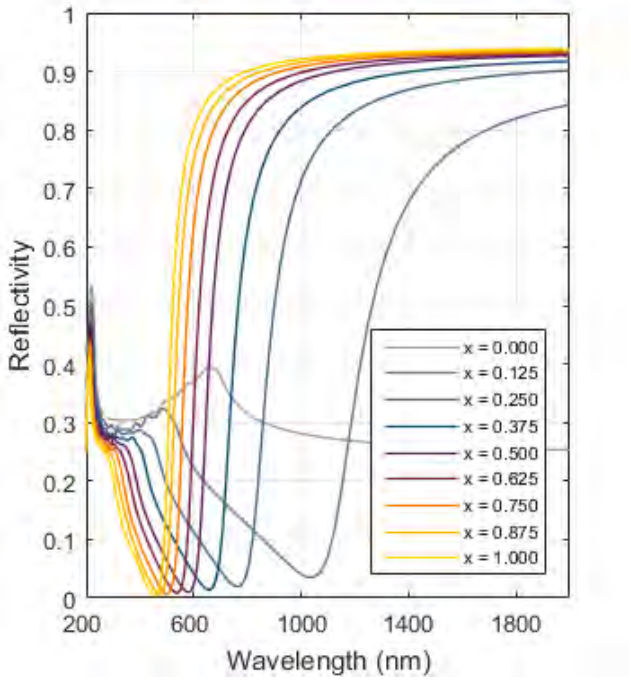

Figure 8. DFT calculated flat-polished normal-incidence reflectivity between $200 \leq \lambda \leq 2000$ nm for c-Na_xWO_3 for $0 \leq x \leq 1$.

The reflectance profiles shown in figure 8 were used to calculate an apparent colour in sRGB colour space. This sRGB triplet was then interpolated over the full $0 \leq x \leq 1$ range, producing the gradient shown in figure 9(a). VLM images of three tungsten bronzes are shown in figure 9(b), (c) and (d), comparing the observed colour to the calculated colour from the gradient. Overall there is good agreement between calculation and experiment, and since small changes in x leads to dramatic changes in hue, these results show that apparent colour offers a fast qualitative method for estimating the sodium content in an unknown sample of Na_xWO_3.

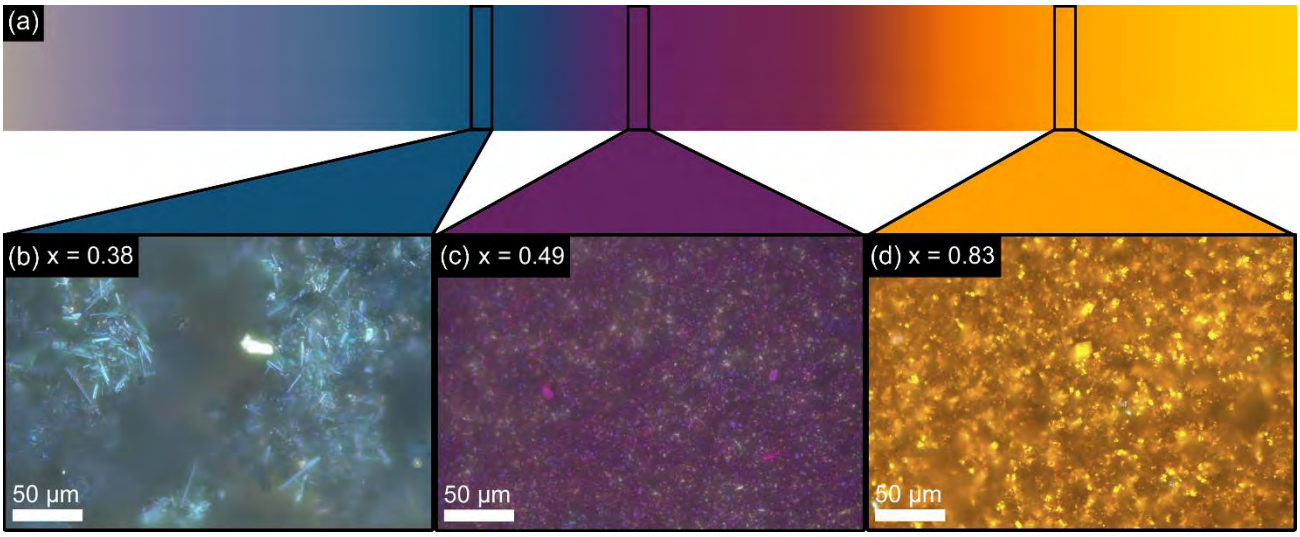

Figure 9. Interpolated sRGB triplets of c-Na_xWO_3 across $0.0 \leq x \leq 1.0$, showing a gradient of calculated approximate visual colours. VLM images of three Na_xWO_3 powders, (b) $x = 0.38$, (c) $x = 0.49$ and (d) $x = 0.83$, are shown with comparison to the calculated colour.

Figure 10 presents calculated bulk electron-energy loss spectra (EELS) for Na_xWO_3 across $0 \leq x \leq 1$. The strong peak around $\omega \approx 2$ eV corresponds to a high quality bulk plasmon, whose magnitude and centre frequency

increases with increasing Na content, approximately following $\omega_{BP} \propto \sqrt{x} \propto \sqrt{N}$ [69]. The $x = 0.000$ curve, corresponding to WO_3, does not have a bulk plasmon peak, which is expected given its semiconductor character. The other peak at $\omega \approx 6.5$ eV arises from the interband transition in the UV, as seen in figure 5. EELS have been measured experimentally on these materials, and has been presented in previous work from this research group [69] and from others [66,70]. In brief, excellent qualitative agreement has been observed between calculated and observed EELS, particularly in the visible frequency range.

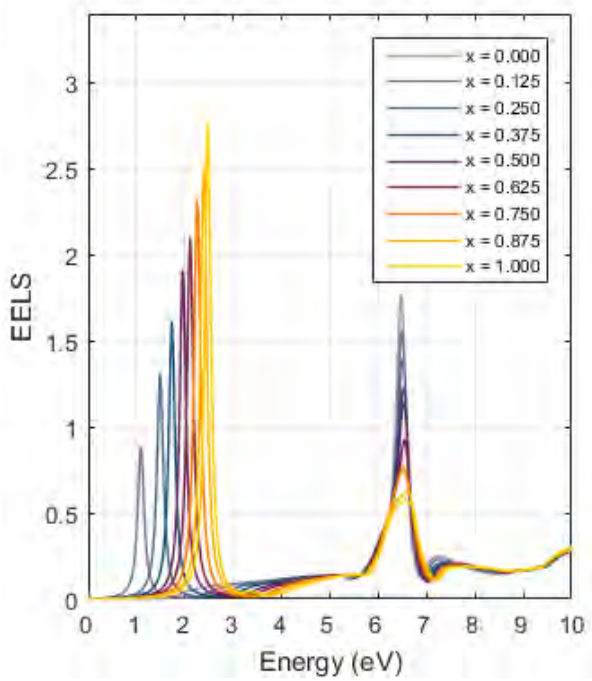

Figure 10. Calculated bulk electron energy-loss spectra (EELS) of c-Na_xWO_3, across $0 \leq x \leq 1$.

The density functional calculations performed here assume a cubic unit cell across all of $0 \leq x \leq 1$, with unbuckled WO_6 octahedra, as in figure 1(b). Phase diagrams from the literature [30] suggest that the cubic unit cell is not usually encountered below $x < 0.4$, instead forming a series of lower-symmetry phases. A density functional investigation by Tosoni *et al.* [21] showed that for WO_3, the cubic approximation has a band gap approximately ≈ 2/3 that of the buckled, monoclinic unit cell found at room temperature. In addition, the use of the PBE-GGA is widely known to underestimate the bandgap [65]. With reference to figure 5, it can be seen that an increase in the band gap for any given stoichiometry is unlikely to reduce the quality of any plasmon resonance, though it may slightly increase the frequency. As discussed, EELS has been performed on the samples fabricated in this work, and it was shown that there is strong agreement between calculation and experiment, especially in the frequencies of bulk and surface plasmons [69]. This suggests that although the bandgap has been underestimated, these calculations are sufficiently accurate to describe the free-electron contribution to the optical properties. Regardless, the calculated optical properties presented in this work are likely most valid for the $x \geq 0.5$ bronzes, with the $x < 0.5$ data included for completeness and to highlight trends.

3.3. Applications in Plasmonics

Figure 11 presents the calculated extinction spectra (σ_{ext}) for a single 20 nm diameter $x = 1.000$ nanocube, immersed in water with $n_{medium} = 1.33$. Peaks in σ_{ext} are labelled (i)-(v), and the corresponding surface electric field magnitudes ($|\boldsymbol{E}|$, top) and surface charge (SC) distributions (bottom) for each peak are shown. The fairly large

Drude broadening (γ_{drude} = 0.15 eV) used in these calculations lead to significant overlap between each extinction peak. To elucidate the LSPR modes, the SC presented for peak (i) was found by subtracting the SC calculated at peak (ii) from the SC calculated at peak (i) (not pictured). Similarly, the SC presented for peak (ii) was found by subtracting the SC at peak (i) from peak (ii) (not pictured). Lastly, the colour range for the SC has been truncated to improve visibility. After these transformations, the peaks in the extinction spectra can easily be identified in terms of LSPRs (peaks i, ii and iii) or interband transitions (iv, v). Peak (i) represents a dipole mode with the electric field and charge focused in the corners of the cube. Peak (ii) represents a quadrupole-like mode, with more charge and electric field concentrated in the edges of the cube. Peak (iii) represents dipole mode with charges focused on opposite faces of the cube, and electric field concentrated at the corresponding edges. Higher order modes form between peaks (ii) and (iii), though are not resolved in these simulations. The $|\boldsymbol{E}|$ and SC maps and peak wavelength ratios closely match those reported in the literature for Ag nanocubes [71–74].

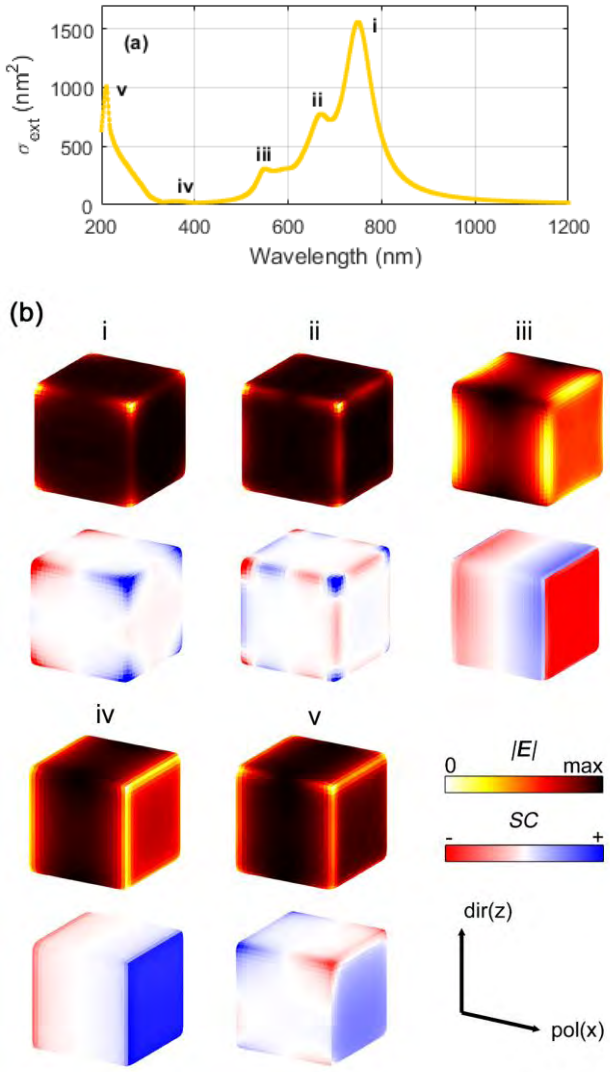

Figure 11. Bright-field modes of a 20 nm nanocube of $Na_{1.000}WO_3$ in water (n_{medium} = 1.33). Five peaks in the extinction spectrum (a) are labelled i-v. (b) presents the corresponding surface electric field magnitude ($|\boldsymbol{E}|$, top) and surface charge distribution (SC, bottom) are shown for each mode. Surface charge maps have had their scales truncated and saturated to improve readability. The direction (dir) and polarization (pol) of the incident planewave are shown bottom right.

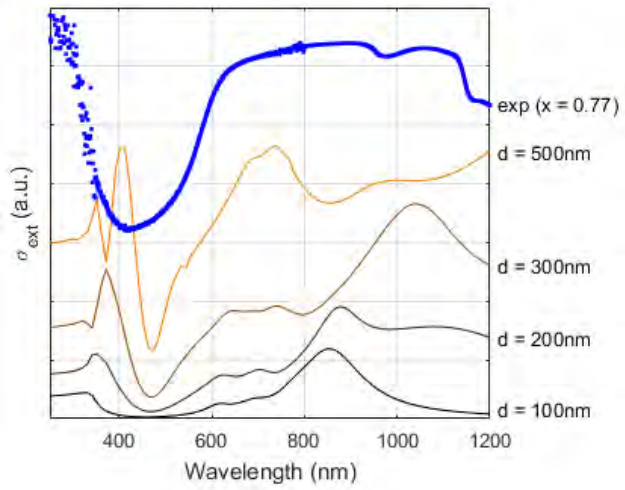

Figure 12. Calculated extinction spectra (σ_{ext}) of $Na_{0.750}WO_3$ nanocubes in water (n_{medium} = 1.33) of varying side length (orange-brown), along with an experimentally obtained σ_{ext} for a $Na_{0.77}WO_3$ bronze (blue).

As several groups in the literature have noted, nanoparticle dispersions of WO_3, sub-stoichiometric $WO_{3-\delta}$ and M_xWO_3 generally exhibit high extinction in the infrared (IR), good transmission in the visible, and some extinction in the ultraviolet (UV) [20,55,60,75,76]. Figure 12 presents the extinction spectra for calculated (x = 0.750) and experimental (x = 0.77) nanoparticle dispersions in water. For the calculated results, extinction spectra were calculated for $Na_{0.75}WO_3$ nanocubes of side length 100 nm, 200 nm, 300 nm and 500 nm immersed in n_{medium} = 1.33. Each of the spectra have been arbitrarily scaled to highlight qualitative trends. In general, increasing the diameter of a nanocube red-shifts the associated LSPRs, as has been reported previously in the literature for the case of Ag [77]. In all of the calculated spectra, an extinction minimum is observed around $\lambda \approx 450$ nm. This minimum is also present in the experimental spectrum, though slightly blue-shifted to $\lambda \approx 400$ nm. The absorption onset in the UV in the calculated spectrum occurs at a longer wavelength than in the experimental due to the underestimate of the band-gap in the calculated $\varepsilon(\omega)$. The experimental spectrum, where the sample was prepared by grinding with a mortar and pestle, will be an average of the extinction spectra from a large range of particles of different sizes. Quantitative comparison between theory and experiment would require knowledge of the particle size distribution, which was not determined in this work. Figure 12 qualitatively demonstrates that the extinction spectra of an ensemble of cubic tungsten bronze particles is consistent with the excitation of LSPR modes on the individual particles. The results support the potential for application of Na_xWO_3 in IR-blocking in solar control window coatings, as has recently been discussed for hexagonal phases of Rb_xWO_3 [60], Cs_xWO_3 [75,78,79], and co-doped $(Li,K)_xWO_3$ [20]. The advantage of the particles prepared in this work over the previous studies is the relative simplicity and scalability of the solid-state synthesis method.

Figure 13 demonstrates the shift in the LSPR wavelength as a function of the refractive index of the external medium for $Na_{0.5}WO_3$, $Na_{1.0}WO_3$, Au and Ag (data from Johnson and Christy [48]). Here, nanospheres and nanocubes with d = 20 nm were immersed in external media defined by a lossless and dispersionless n_{medium}. The extinction spectra of these nanoparticles were calculated, and the wavelength of the strongest LSPR peak has been plotted against $n_{medium.}$ For the spheres, this was the dipole mode, whilst for the cubes, this was the corner-dipole mode (peak (i) in figure 11). For all materials, there is an overall redshift of the plasmon resonance as n_{medium} is

increased as expected. However, it can be seen that the magnitude of the redshift is greatest for the $Na_{0.5}WO_3$ nanocube, shifting $\Delta\lambda_{LSPR}$ = 338.20 nm per refractive-index-unit (RIU) of n_{medium}, whereas the Au nanocube shifts just $\Delta\lambda_{LSPR}$ = 130.27 nm.RIU^{-1}. The data presented in figure 13 is summarized in Table 3. Investigations into the shift of the λ_{LSPR} with varying n_{medium} can be found in the literature for both Au/Ag nanospheres [80–82] and nanocubes [72,83,84], which have produced similar numerical values to those presented here. Slight differences in λ_{LSPR} in the case of nanocubes can be attributed to edge and corner rounding, which dramatically shift the wavelengths of the corner and edge modes [73,77]. These results have important consequences in chemical sensing applications, which rely on a shift in refractive index with changes in the chemical environment. Substituting $Na_{0.5}WO_3$ nanoparticles for Au or Ag nanoparticles in such systems will roughly double the wavelength shift for any given change in n_{medium}, greatly increasing sensitivity.

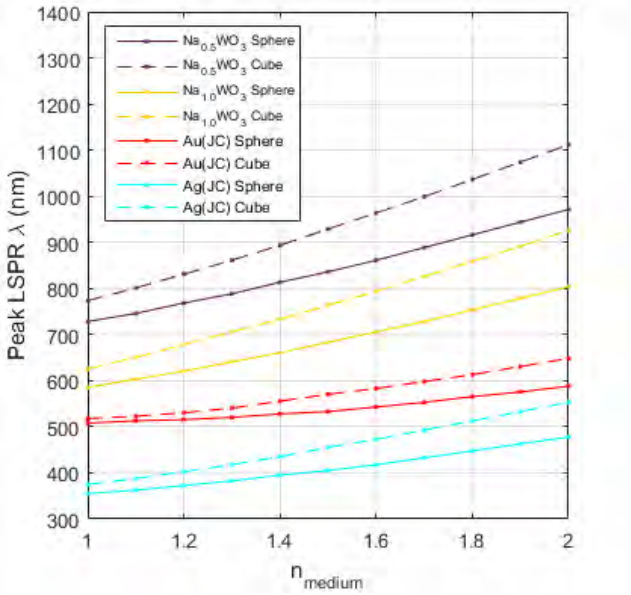

Figure 13. The calculated wavelength-shift of the peak plasmon resonance with increasing n_{medium} for 20 nm spheres and cubes of $Na_{0.5}WO_3$, $Na_{1.0}WO_3$, Au and Ag (data from Johnson and Christy [48]). This data is summarized in Table 3.

Table 3. Shifts in peak LSPR wavelengths for nanospheres and nanocubes as the refractive index of the external medium (n_{medium}) is increased from n_{medium} = 1 to n_{medium} = 2 for $Na_{0.5}WO_3$, $Na_{1.0}WO_3$, Au and Ag.

$\Delta\lambda_{LSPR}$.RIU^{-1} (n_{medium} = 1 → 2)		
Material	**20 nm sphere**	**20 nm cube**
$Na_{0.5}WO_3$	243.00 nm	338.20 nm
$Na_{1.0}WO_3$	217.95 nm	300.63 nm
Au	80.17 nm	130.27 nm
Ag	122.76 nm	177.87 nm

One promising aspect of the tungsten bronzes as plasmonic materials is the tunability of the LSPR by composition, in addition to particle geometry. Figure 14(a) shows σ_{ext} of 60 nm nanocubes of c-Na_xWO_3 of x = 0.500, x = 0.750 and x = 1.000, alongside the σ_{ext} for an Au 60×15 nm (aspect ratio 4:1) cylindrical nanorod (data from Johnson and Christy [48]). In (e), σ_{ext} is shown for cylindrical nanorods of c-$Na_{0.5}WO_3$ of increasing aspect ratio (length:diameter, see (d)). Simulations were performed with the incident wave being polarized both parallel and

perpendicular to the long-axis of the rod, as shown in (c). The two spectra were then summed to give the spectra plotted in (a) and (e). The particles are simulated as being immersed in water, and the locations of two near-infrared (NIR) biological windows are overlaid [85]. For conventional plasmonic materials such as Au or Ag, control of the LSPR wavelength comes from control of particle geometry, where LSPRs can be red-shifted by reducing particle symmetry or by increasing particle size. From (a), it can be seen that, for a fixed particle size and shape, an increase in Na content leads to a dramatic blue-shift of the resonances. This is useful in the context of plasmonics for some biomedical applications, whereby extinction peaks need to lie in the biological NIR window(s), which represent wavelength regions of minimum attenuation and scattering from biological materials [2,85,86]. Spherical Au nanoparticles in water typically resonate around $\lambda_{LSPR} \approx 550$ nm (see figure 13), so in order to red-shift the resonance, lower-symmetry nanoparticles such as nanorods have been fabricated [2]. Figure 14 shows that the tuneable and intrinsically lower plasma frequency of the sodium tungsten bronzes, combined with the natural tendency to form nanocubes (see section 3.1.), means that providing the particles can be made small enough (< 100 nm), the sodium tungsten bronzes can be made resonant in the biological NIR window. The use of tungsten bronzes as photothermal ablation therapy agents has previously been reported in the literature for nanorods of Cs_xWO_3 [87] and Rb_xWO_3 [88], and for nanocubes of $(NH_4)_xWO_3$ [56]. Work is underway to optimize the solid-state synthesis methods to reduce the c-Na_xWO_3 particle sizes.

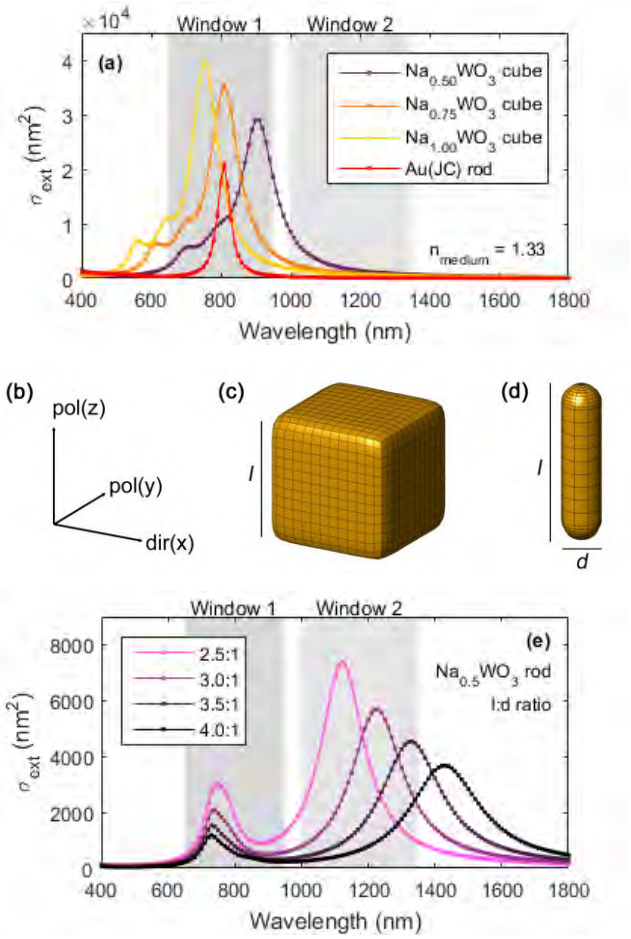

Figure 14. Extinction spectra (σ_{ext}) for (a) 60 nm nanocubes of $Na_{0.5}WO_3$, $Na_{0.75}WO_3$ and $Na_{1.0}WO_3$, and a 60×15 nm cylindrical nanorod of Au (data from Johnson and Christy [48]). (b) shows the direction (x) and polarization states (y, z) of the incident planewaves for these simulations. (c) shows a model of a nanocube with side length l, and (d) shows a nanorod with length l and diameter d. (e) plots extinction spectra of cylindrical nanorods of $Na_{0.5}WO_3$ of fixed length (l = 60 nm), and

varying diameter (d) and aspect ratio (l:d). All particles are simulated in water. The two NIR biological windows, one across $650 \leq \lambda \leq 950$ nm and the other across $1000 \leq \lambda \leq 1350$ nm [85], are overlaid in grey.

Though they have not been experimentally realized, the extinction spectra for cylindrical nanorods 60 nm long of c-$Na_{0.5}WO_3$ with varying aspect ratio are shown in figure 14(b). For rods of aspect ratio 4:1 (60×15 nm), the longitudinal mode sits to the long-wavelength side of the second biological NIR window ($\lambda \approx 1450$ nm), whilst the transverse mode sits near the centre of the first biological NIR window ($\lambda \approx 750$ nm). By reducing the aspect ratio, the longitudinal mode blueshifts, such that when the aspect ratio is approximately ≈ 2.5:1 (≈ 60×24 nm), the transverse mode remains in window 1, and the longitudinal mode sits in the middle of window 2. This suggests that a single well-designed Na_xWO_3 nanorod ensemble can be used with either window, increasing the versatility of photothermal ablation techniques. The observation of needle-like structures for Na_xWO_3 when $x \approx 0.4$ indicates Na_xWO_3 nanorod formation is possible.

In general, Ag has optical properties superior to both Au and Na_xWO_3 across the full range of wavelengths studied. However, the high reactivity and rapid corrosion of Ag means that Au is more widely used in atmospheric or biological environments. The results presented here suggest that the sodium tungsten bronzes possess optical properties as good as and, for some purposes, better than Au, but without the reactivity of Ag. In addition, the wavelength of the LSPR is tuneable not only by nanoparticle geometry but also by chemical composition. The ability to tune optical properties by Na content could allow the fine-tuning of optical properties in applications where there may be restrictions on nanostructure, such as in nanoplasmonic waveguides [89]. These results indicate that the sodium tungsten bronzes have excellent potential to replace Ag or Au as plasmonic materials in some applications.

4. Conclusions

In this work, we have shown that the cubic phases of sodium tungsten bronzes (c-Na_xWO_3) have potential as plasmonic materials. Through a simple solid state reaction, well-formed nanocubes of diameters ≥1 μm were formed for $x > 0.5$ bronzes. Using DFT and BEM, the bulk and nanoscale optical properties of the bronzes were calculated, and showed performance similar to or better than Au or Ag in some applications, in particular in chemical sensing and biomedical applications. The sodium tungsten bronze's strengths over existing plasmonic materials are their low chemical reactivity, the intrinsically low ($x = 1.0$, $\omega_p = 2.49$ eV) and tuneable bulk plasma frequency, and high sensitivity of LSPR wavelength with changes in the external medium refractive index (high $\Delta\lambda_{LSPR}.RIU^{-1}$). Work is ongoing in optimising fabrication parameters to enable the bulk production of phase-pure sodium tungsten bronze nanoparticles.

Acknowledgements

This research was supported under Australian Research Council's Discovery Projects funding scheme (Project Number DP120102545). The Priority Research Centre for Organic Electronics (PRCOE) at The University of Newcastle is thanked for access to optical spectroscopy. The technical support of J. Zobec is acknowledged.

References

[1] Atwater H A and Polman A 2010 Plasmonics for improved photovoltaic devices *Nat. Mater.* **9** 205–13

[2] Jain P K, Huang X, El-Sayed I H and El-Sayed M A 2007 Review of Some Interesting Surface Plasmon Resonance-enhanced Properties of Noble Metal Nanoparticles and Their Applications to Biosystems *Plasmonics* **2** 107–18

[3] Brolo A G 2012 Plasmonics for future biosensors *Nat. Photonics* **6** 709–13

[4] Zeng S, Baillargeat D, Ho H-P and Yong K-T 2014 Nanomaterials enhanced surface plasmon resonance for biological and chemical sensing applications *Chem. Soc. Rev.* **43** 3426–52

[5] Zhang X, Chen Y L, Liu R-S and Tsai D P 2013 Plasmonic photocatalysis *Rep. Prog. Phys.* **76** 046401

[6] Arnold M D and Blaber M G 2009 Optical performance and metallic absorption in nanoplasmonic systems *Opt. Express* **17** 3835

[7] Naik G V, Shalaev V M and Boltasseva A 2013 Alternative Plasmonic Materials: Beyond Gold and Silver *Adv. Mater.* **25** 3264–94

[8] West P R, Ishii S, Naik G V, Emani N K, Shalaev V M and Boltasseva A 2010 Searching for better plasmonic materials *Laser Photonics Rev.* **4** 795–808

[9] Comin A and Manna L 2014 New materials for tunable plasmonic colloidal nanocrystals *Chem. Soc. Rev.* **43** 3957–75

[10] Zhong Y, Malagari S D, Hamilton T and Wasserman D 2015 Review of mid-infrared plasmonic materials *J. Nanophotonics* **9** 093791–093791

[11] Keast V J, Barnett R L and Cortie M B 2014 First principles calculations of the optical and plasmonic response of Au alloys and intermetallic compounds *J. Phys. Condens. Matter* **26** 305501

[12] Bobb D A, Zhu G, Mayy M, Gavrilenko A V, Mead P, Gavrilenko V I and Noginov M A 2009 Engineering of low-loss metal for nanoplasmonic and metamaterials applications *Appl. Phys. Lett.* **95** 151102

[13] Blaber M G, Arnold M D and Ford M J 2010 A review of the optical properties of alloys and intermetallics for plasmonics *J. Phys. Condens. Matter* **22** 143201

[14] Boltasseva A and Shalaev V M 2015 All that glitters need not be gold *Science* **347** 1308–10

[15] Gui L, Bagheri S, Strohfeldt N, Hentschel M, Zgrabik C M, Metzger B, Linnenbank H, Hu E L and Giessen H 2016 Nonlinear Refractory Plasmonics with Titanium Nitride Nanoantennas *Nano Lett.*

[16] Otsuji T, Popov V and Ryzhii V 2014 Active graphene plasmonics for terahertz device applications *J. Phys. Appl. Phys.* **47** 094006

[17] Naik G V and Boltasseva A 2010 Semiconductors for plasmonics and metamaterials *Phys. Status Solidi RRL – Rapid Res. Lett.* **4** 295–7

[18] Rajak S and Ray M 2014 Comparative study of plasmonic resonance in transparent conducting oxides: ITO and AZO *J. Opt.* **43** 231–8

[19] Frigerio J, Ballabio A, Isella G, Sakat E, Pellegrini G, Biagioni P, Bollani M, Napolitani E, Manganelli C, Virgilio M, Grupp A, Fischer M P, Brida D, Gallacher K, Paul D J, Baldassarre L, Calvani P, Giliberti V, Nucara A and Ortolani M 2016 Tunability of the dielectric function of heavily doped germanium thin films for mid-infrared plasmonics *Phys. Rev. B* **94** 085202

[20] Yang C, Chen J-F, Zeng X, Cheng D, Huang H and Cao D 2016 Enhanced near-infrared shielding ability of (Li,K)-codoped WO 3 for smart windows: DFT prediction validated by experiment *Nanotechnology* **27** 075203

[21] Tosoni S, Di Valentin C and Pacchioni G 2014 Effect of Alkali Metals Interstitial Doping on Structural and Electronic Properties of WO3 *J. Phys. Chem. C* **118** 3000–6

[22] Magnéli A and Blomgberg B 1951 Contrubtion to the Knowledge of the Alkalai Tungsten Bronzes *Acta Chem. Scand.* **5** 372–278

[23] Straumanis M E 1949 The Sodium Tungsten Bronzes. I. Chemical Properties and Structure *J. Am. Chem. Soc.* **71** 679–83

[24] Brown B W and Banks E 1954 The Sodium Tungsten Bronzes *J. Am. Chem. Soc.* **76** 963–6

[25] El-Sayed A M and Mousa S M A 2005 Some properties of sodium tungsten bronzes as a fuction of sodium concentration *Indian J. Chem. Technol.* **12** 304–8

[26] Bevan D J M and Hagenmuller P 1975 *Nonstoichiometric Compounds: Tungsten Bronzes, Vanadium Bronzes and Related Compounds* (Great Britain: Elsevier)

[27] Raj S, Matsui H, Souma S, Sato T, Takahashi T, Chakraborty A, Sarma D D, Mahadevan P, Oishi S, McCarroll W H and Greenblatt M 2007 Electronic structure of sodium tungsten bronzes NaxWO3 by high-resolution angle-resolved photoemission spectroscopy *Phys. Rev. B* **75** 155116

[28] Wiseman P J and Dickens P G 1976 Neutron diffraction studies of cubic tungsten bronzes *J. Solid State Chem.* **17** 91–100

[29] Clarke R 1977 New Sequence of Structural Phase Transitions in NaxWO3 *Phys. Rev. Lett.* **39** 1550–3

[30] Ribnick A S, Post B and Banks E 1963 Phase Transitions in Sodium Tungsten Bronzes ed R Ward *Nonstoichiom. Compd.* **39** 246–53

[31] Magnéli A, Mårin R, Haug C M, Stene J and Sörensen N A 1951 Tetragonal Tungsten Bronzes of Degenerated Perovskite Type. *Acta Chem. Scand.* **5** 670–2

[32] Takusagawa F and Jacobson R A 1976 Crystal structure studies of tetragonal sodium tungsten bronzes, NaxWO3. I. Na0.33WO3 and Na0.48WO3 *J. Solid State Chem.* **18** 163–74

[33] Gao T and Jelle B P 2013 Visible-Light-Driven Photochromism of Hexagonal Sodium Tungsten Bronze Nanorods *J. Phys. Chem. C* **117** 13753–61

[34] Martins T A, Machado T R, Ferrer M M, Zanetti S M and Longo E 2016 Facile microwave-assisted hydrothermal synthesis of hexagonal sodium tungsten bronze and its high response to NO2 *Mater. Lett.* **185** 197–200

[35] Inorganic Crystal Structure Database (ICSD) - FIZ Karlsruhe, https://icsd.fiz-karlsruhe.de/ (accessed 15 November 2016)

[36] The International Centre for Diffraction Data (ICDD), http://www.icdd.com/, (accessed 15 November 2016)

[37] B A Hunter and C J Howard 2016 Rietica (version 4.2)

[38] Hunter B A and Howard C J 2016 *LHPM: A computer program for Rietveld analysis of X-ray and neutron powder diffraction patterns* (NSW Australia: ANSTO)

[39] Schwarz K 2003 DFT calculations of solids with LAPW and WIEN2k *J. Solid State Chem.* **176** 319–28

[40] Perdew J P, Burke K and Ernzerhof M 1996 Generalized Gradient Approximation Made Simple *Phys. Rev. Lett.* **77** 3865–8

[41] Ambrosch-Draxl C and Sofo J O 2006 Linear optical properties of solids within the full-potential linearized augmented planewave method *Comput. Phys. Commun.* **175** 1–14

[42] Owen J F, Teegarden K J and Shanks H R 1978 Optical properties of the sodium-tungsten bronzes and tungsten trioxide *Phys. Rev. B* **18** 3827–37

[43] Camagni P, Manara A, Campagnoli G, Gustinetti A and Stella A 1977 Optical properties of metallic sodium tungsten bronzes: Analysis of free- and bound-electron contributions *Phys. Rev. B* **15** 4623–30

[44] ASTM E308-01 2001 Standard Practice for Computing the Colors of Objects by Using the CIE System, American Society for Testing and Materials

[45] Hohenester U and Trügler A 2012 MNPBEM – A Matlab toolbox for the simulation of plasmonic nanoparticles *Comput. Phys. Commun.* **183** 370–81

[46] Waxenegger J, Trügler A and Hohenester U 2015 Plasmonics simulations with the MNPBEM toolbox: Consideration of substrates and layer structures *Comput. Phys. Commun.* **193** 138–50

[47] García de Abajo F J and Howie A 2002 Retarded field calculation of electron energy loss in inhomogeneous dielectrics *Phys. Rev. B* **65** 115418

[48] Johnson P B and Christy R W 1972 Optical Constants of the Noble Metals *Phys. Rev. B* **6** 4370–9

[49] Okada K, Morikawa H, Marumo F and Iwai S 1975 Disodium ditungstate *Acta Crystallogr. B* **31** 1200–1

[50] Okada K, Morikawa H, Marumo F and Iwai S 1974 Sodium tungstate *Acta Crystallogr. B* **30** 1872–3

[51] Viswanathan K 1974 Crystal structure of sodium tetratungstate, Na2W4O13 *J. Chem. Soc., Dalton Trans.* 2170–2

[52] Dickens P G and Whittingham M S 1968 The tungsten bronzes and related compounds *Q. Rev. Chem. Soc.* **22** 30–44

[53] Paul S, Kumari S and Raj S 2016 High-resolution angle-resolved photoemission investigation of potassium and phosphate tungsten bronzes *J. Electron Spectrosc. Relat. Phenom.* **208** 67–73

[54] Yue S and Zhang Y 2012 Electronic Transport Properties of Sodium Tungsten Bronzes Na0.54WO3 Single Crystals *J. Mater. Sci. Technol.* **28** 569–71

[55] Eyassu T, Hsaio T-J and Lin C-T 2015 Facile solvothermal synthesis of NIR absorbing Cs x WO 3 nanorods by benzyl alcohol route *Mater. Res. Express* **2** 015016

[56] Guo C, Yu H, Feng B, Gao W, Yan M, Zhang Z, Li Y and Liu S 2015 Highly efficient ablation of metastatic breast cancer using ammonium-tungsten-bronze nanocube as a novel 1064 nm-laser-driven photothermal agent *Biomaterials* **52** 407–16

[57] Mattox T M, Bergerud A, Agrawal A and Milliron D J 2014 Influence of Shape on the Surface Plasmon Resonance of Tungsten Bronze Nanocrystals *Chem. Mater.* **26** 1779–84

[58] Guo J, Dong C, Yang L and Fu G 2005 A green route for microwave synthesis of sodium tungsten bronzes NaxWO3 (0<x<1) *J. Solid State Chem.* **178** 58–63

[59] Azimirad R, Akhavan O and Moshfegh A Z 2009 Simple Method to Synthesize NaxWO3 Nanorods and Nanobelts *J. Phys. Chem. C* **113** 13098–102

[60] Wu X, Wang J, Zhang G, Katsumata K, Yanagisawa K, Sato T and Yin S 2017 Series of MxWO3/ZnO (M = K, Rb, NH4) nanocomposites: Combination of energy saving and environmental decontamination functions *Appl. Catal. B Environ.* **201** 128–36

[61] Wei Q, Shi H, Cheng X, Qin L, Ren G and Shu K 2010 Growth and scintillation properties of the Na2W2O7 crystal *J. Cryst. Growth* **312** 1883–5

[62] Ross-Medgaarden E I and Wachs I E 2007 Structural Determination of Bulk and Surface Tungsten Oxides with UV−vis Diffuse Reflectance Spectroscopy and Raman Spectroscopy *J. Phys. Chem. C* **111** 15089–99

[63] Ingham B, Hendy S C, Chong S V and Tallon J L 2005 Density-functional studies of tungsten trioxide, tungsten bronzes, and related systems *Phys. Rev. B* **72** 075109

[64] Paul S, Kumari S and Raj S 2016 Vacancy-induced in-gap states in sodium tungsten bronzes: Density functional investigations *EPL Europhys. Lett.* **114** 37011

[65] V J Keast 2016 Transmission Electron Micoscopy: Diffraction, Imaging and Spectrometry, ed C B Carter and D B Williams (Cham Switzerland: Springer International Publishing) p 518

[66] Kielwein M, Saiki K, Roth G, Fink J, Paasch G and Egdell R G 1995 High-energy electron-energy-loss study of sodium-tungsten bronzes *Phys. Rev. B* **51** 10320–35

[67] Bullett D W 1983 Bulk and surface electron states in WO3 and tungsten bronzes *J. Phys. C Solid State Phys.* **16** 2197–207

[68] Xue Y, Zhang Y and Zhang P 2009 Theory of the color change of NaxWO3 as a function of Na-charge doping *Phys. Rev. B* **79** 205113

[69] Tegg L, Cuskelly D and Keast V J 2017 Plasmon Responses in the Sodium Tungsten Bronzes *Plasmonics* 1–8

[70] Dietz R E, Campagna M, Chazalviel J N and Shanks H R 1978 Inelastic electron scattering by intra- and interband plasmons in rhenium trioxide, tungsten trioxide, and some tungsten bronzes *Phys. Rev. B* **17** 3790–800

[71] Zhou F, Li Z-Y, Liu Y and Xia Y 2008 Quantitative Analysis of Dipole and Quadrupole Excitation in the Surface Plasmon Resonance of Metal Nanoparticles *J. Phys. Chem. C* **112** 20233–40

[72] Zhang S, Bao K, Halas N J, Xu H and Nordlander P 2011 Substrate-Induced Fano Resonances of a Plasmonic Nanocube: A Route to Increased-Sensitivity Localized Surface Plasmon Resonance Sensors Revealed *Nano Lett.* **11** 1657–63

[73] Grillet N, Manchon D, Bertorelle F, Bonnet C, Broyer M, Cottancin E, Lermé J, Hillenkamp M and Pellarin M 2011 Plasmon Coupling in Silver Nanocube Dimers: Resonance Splitting Induced by Edge Rounding *ACS Nano* **5** 9450–62

[74] Near R, Hayden S and El-Sayed M 2012 Extinction vs Absorption: Which Is the Indicator of Plasmonic Field Strength for Silver Nanocubes? *J. Phys. Chem. C* **116** 23019–26

[75] Adachi K and Asahi T 2012 Activation of plasmons and polarons in solar control cesium tungsten bronze and reduced tungsten oxide nanoparticles *J. Mater. Res.* **27** 965–970

[76] Takeda H and Adachi K 2007 Near Infrared Absorption of Tungsten Oxide Nanoparticle Dispersions *J. Am. Ceram. Soc.* **90** 4059–61

[77] Hung L, Lee S Y, McGovern O, Rabin O and Mayergoyz I 2013 Calculation and measurement of radiation corrections for plasmon resonances in nanoparticles *Phys. Rev. B* **88** 075424

[78] Guo C, Yin S, Zhang P, Yan M, Adachi K, Chonan T and Sato T 2010 Novel synthesis of homogenous CsxWO3 nanorods with excellent NIR shielding properties by a water controlled-release solvothermal process *J. Mater. Chem.* **20** 8227–9

[79] Liu J, Xu Q, Shi F, Liu S, Luo J, Bao L and Feng X 2014 Dispersion of Cs0.33WO3 particles for preparing its coatings with higher near infrared shielding properties *Appl. Surf. Sci.* **309** 175–80

[80] Chen H, Kou X, Yang Z, Ni W and Wang J 2008 Shape- and Size-Dependent Refractive Index Sensitivity of Gold Nanoparticles *Langmuir* **24** 5233–7

[81] Sekhon J S and Verma S S 2011 Refractive Index Sensitivity Analysis of Ag, Au, and Cu Nanoparticles *Plasmonics* **6** 311–7

[82] Lee K-S and El-Sayed M A 2006 Gold and Silver Nanoparticles in Sensing and Imaging: Sensitivity of Plasmon Response to Size, Shape, and Metal Composition *J. Phys. Chem. B* **110** 19220–5

[83] Ahamad N, Bottomley A and Ianoul A 2012 Optimizing Refractive Index Sensitivity of Supported Silver Nanocube Monolayers *J. Phys. Chem. C* **116** 185–92

[84] Lee Y H, Chen H, Xu Q-H and Wang J 2011 Refractive Index Sensitivities of Noble Metal Nanocrystals: The Effects of Multipolar Plasmon Resonances and the Metal Type *J. Phys. Chem. C* **115** 7997–8004

[85] Smith A M, Mancini M C and Nie S 2009 Bioimaging: Second window for in vivo imaging *Nat. Nanotechnol.* **4** 710–1

[86] Jain P K, El-Sayed I H and El-Sayed M A 2007 Au nanoparticles target cancer *Nano Today* **2** 18–29

[87] Guo C, Yin S, Yu H, Liu S, Dong Q, Goto T, Zhang Z, Li Y and Sato T 2013 Photothermal ablation cancer therapy using homogeneous CsxWO3 nanorods with broad near-infra-red absorption *Nanoscale* **5** 6469–78

[88] Tian G, Zhang X, Zheng X, Yin W, Ruan L, Liu X, Zhou L, Yan L, Li S, Gu Z and Zhao Y 2014 Multifunctional RbxWO3 Nanorods for Simultaneous Combined Chemo-photothermal Therapy and Photoacoustic/CT Imaging *Small* **10** 4160–70

[89] Fang Y and Sun M 2015 Nanoplasmonic waveguides: towards applications in integrated nanophotonic circuits *Light Sci. Appl.* **4** e294